Two-Axis Electromagnetic Scanner Using an Asymmetric Frame on a One-Axis Lateral Magnetic Field

Yuki Okamoto, *Member, IEEE*, Rihachiro Nakashima, *Graduate Student Member, IEEE*, Ryo Oda, Thanh-Vinh Nguyen, Yusuke Takei, *Member, IEEE*, Masaaki Ichiki, and Hironao Okada

***Abstract*— Conventional electromagnetic microelectromechanical system scanners require a biaxial (two-axis) external magnetic field to obtain a biaxial torque, which increases the number of bulky external permanent magnets and the packaging size caused by 45°-orientated placement of permanent magnets. Thus, this study developed a two-axis resonant electromagnetic scanner with an asymmetric gimbal frame that generates two-axis torque via a one-axis lateral external magnetic field. As external permanent magnets can be placed parallel to the device die, the proposed method reduced the packaging size. Two driving forces were generated by two independent electromagnetic actuators placed on both sides of the asymmetric gimbal frame, which converted the unidirectional forces into two-axis torque. As the two driving actuators were independent of the connecting beams, gimbal frame, and mirror and were connected to the thick outer Si handle frame, the temperature increase of torsion beams and the asymmetric gimbal frame, which affects the resonant performance, were reduced. Additionally, as the current paths were not multiturn coil shapes, the paths can be formed with a via-less single metal layer. Also, the drive circuit can be simplified since drive signals for two-axis rotation can be applied to individual actuators. We demonstrated biaxial scanning using the proposed structure with a 4-mm mirror. The optical scanning angle was 4.84° for the 1.308 kHz X-axis scan and 16.1° for the 2.568 kHz Y-axis scan when a current of 300 mA was applied independently to the X- and Y-axes driving actuators. We obtained the large displacement at the resonant frequency using the asymmetric gimbal frame under a lateral magnetic field. [2024-0050]**

***Index Terms*— LiDAR, electromagnetic, scanner, mirror.**

I. Introduction

MICROELECTROMECHANICAL systems (MEMS)-based scanners have become essential for laser scanning because of their compact sizes and fast responses [1]. Exploiting these advantages, MEMS scanners have been integrated into various applications, such as three-dimensional (3D) imaging [2], small projectors (known as pico projectors) [3], and light detection and ranging (LiDAR) [1], [4]. LiDAR applications require a high-performance MEMS scanner with a large scanning angle, large mirror, and fast response [1], [5], [6], [7]. Among the many actuation principles such as the electrostatic [8] and piezoelectric [9], [10], [11] principles,

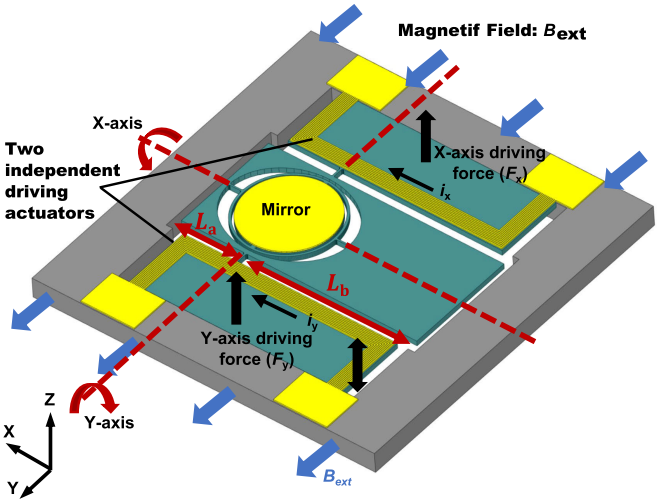

Fig. 1. Schematic of the proposed two-axis electromagnetic scanner with an asymmetric gimbal frame.

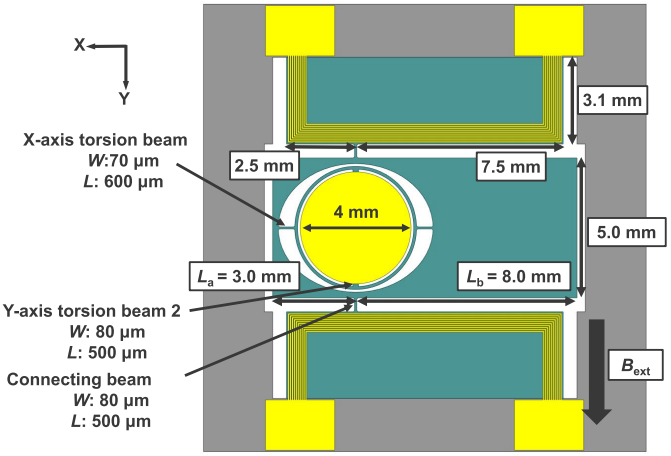

Fig. 2. Design and dimensions of the proposed two-axis electromagnetic scanner.

Manuscript received 28 February 2024; revised 12 May 2024; accepted 14 May 2024. Date of publication 29 May 2024; date of current version 2 August 2024. This work was supported by JSPS KAKENHI Grant Numbers JP20K22422 and 21K14219. Subject Editor N. Quack. *(Corresponding author: Yuki Okamoto.)*

Yuki Okamoto, Thanh-Vinh Nguyen, Yusuke Takei, Masaaki Ichiki, and Hironao Okada are with the Sensing System Research Center, National Institute of Advanced Industrial Science and Technology (AIST), Tsukuba, Ibaraki 305-8564, Japan (e-mail: yuki.okamoto@aist.go.jp).

Rihachiro Nakashima and Ryo Oda are with the Department of Mechanical Engineering, Faculty of Science and Technology, Keio University, Yokohama, Kanagawa 223-8522, Japan.

Color versions of one or more figures in this article are available at https://doi.org/10.1109/JMEMS.2024.3402211.

Digital Object Identifier 10.1109/JMEMS.2024.3402211

TABLE I
COMPARISON OF PREVIOUS ELECTROMAGNETIC SCANNERS AND THIS WORK

	Cho [13]	Koh [17]	This work
X-Scanning method	Electromagnetic	Electromagnetic	Electromagnetic
Y-Scanning method	Electromagnetic	Electrothermal (Slow)	Electromagnetic
Required Magnetic Field	Two-axis	One-axis	One-axis
Current-path structure	Multi-level Via-required	Multi-level Via-required	Single-level Via-less
Current-path position	In gimbal frame (Thermally isolated from the Si handle frame)	In gimbal frame (Thermally isolated from the Si handle frame)	Not in gimbal (Connected to the Si handle frame)

electromagnetic actuators are widely used as driving actuators in a MEMS scanner. In electromagnetic actuation, the use of multiturn coils in the moving part as current paths and external permanent magnets in the housing are essential for generating the Lorentz force. Conventional electromagnetic MEMS scanners require a biaxial (two-axis) external magnetic field to obtain a biaxial torque [12]. This requirement increases the number of bulky external permanent magnets or decomposes a one-axis magnetic field into a two-axis magnetic field via a 45°-orientated placement of permanent magnets [13], [14], [15].

When such a 45°-oriented magnetic field is used, a square MEMS scanner chip must be placed at 45° for packaging between a pair of permanent magnets. In other words, the packaging area must be 1.41 times the device's size and the external magnet's size. As a result, it is challenging to reduce the packaging area [16]. In addition, driving multiturn coils must be placed on a gimbal with 2 degrees-of-freedom connected only by narrow beams in the conventional electromagnetic MEMS scanner. Such a structure increases the temperature rise of the mirror and torsional beams since the generated heat can hardly dissipate through the thick outer Si handle frame.

Although certain studies have solved this issue using a radial magnetic field under a scanner [17] or by combining other principal actuators [18], these methods still limit the scanning angle simply because when the rotation angle is too large, the mirror hits the permanent magnet on the back. Therefore, reducing the number of external permanent magnets remains an issue for realizing high-performance compact 2D MEMS scanners.

Another issue is the multiturn coils in a gimbal. These coils require vertical-interconnect-access (via) fabrication of current paths by multi-metal layers. Although such a multilayer interconnection can be realized through standard MEMS and CMOS processes, it complicates the fabrication. Moreover, the multiturn coils must be placed on a gimbal with 2 degrees-of-freedom connected only by narrow beams, it is challenging for Joule heating to dissipate from the gimbal and mirror, causing performance degradation and mirror deformation.

This study proposed a novel two-axis resonant electromagnetic scanner with an asymmetric gimbal frame to solve these issues [19], [20]. In the proposed scanner, two-axis torques were mechanically generated via an asymmetric gimbal frame using only a one-axis lateral magnetic field, as shown in Figs. 1 and 2. Although Chen et al. used a asymmetric frame and Y-shaped bulk Pb(Zr, Ti)O_3 (PZT) actuators for two-axis piezoelectric MEMS scanner [9], their proposed structure required an adder circuit and two signals in each of the two-axis rotation with different phase differences between the two pairs of PZT plates in the Y-shaped actuator. In our proposed method, two driving forces were generated by two independent actuators placed on both sides of the asymmetric gimbal frame, which converted the unidirectional forces into two-axis torque. Therefore, the drive circuit can be simplified since drive signals for two-axis rotation can be applied to individual actuators. In addition, external permanent magnets were placed laterally, and the two independent driving actuators required only a one-axis magnetic field. Furthermore, two current paths were independent of the connecting beams, gimbal frame, and mirror. Compared to previous studies in Table I, this facilitated the use of a simpler via-less fabrication and avoided Joule heating of the mirror. In this paper, we first discussed how the proposed asymmetric framework works. Then, simulation results showed the proposed scanner's characteristics. Finally, we fabricated and demonstrated the proposed scanner.

II. METHODOLOGY

Figure 2 shows the design of the proposed two-axis scanning mirror with an asymmetric gimbal frame. The mirror frame and actuators were composed of a 40-μ m thick device layer of a 40/1/400 μ m silicon-on-insulator (SOI) wafer. The size of the device die was 2×2 cm^2 and the diameter of the mirror was 4 mm. As shown in Fig. 2, the mirror frame was designed asymmetrically on the Y-axis to generate two-axis torque from a one-axis lateral magnetic field (B_{ext}). The shorter and longer parts of the asymmetric gimbal frame were L_{a} and L_{b}, respectively, where $L_{\text{a}} < L_{\text{b}}$. The electrodes on the two actuators were made up of 200-nm thick gold and 15-nm titanium. The length, width and gap of the current paths are 2000, 200 and 50 μ m, respectively. Because the two current paths on the two independently driven actuators were fully isolated, the two driving currents (i_{x} and i_{y}) could be applied independently without any crosstalk.

Two electromagnetic actuators were placed on both sides of the mirror frame to generate vertical electromagnetic forces (F_{x} and F_{y}) from B_{ext}. Figures 3(a) and 3(b) show X- and Y-axes rotation schematics, respectively. The vertical X-axis rotation directly utilized the force, as shown in Fig. 3(a). Whereas, the horizontal Y-axis rotation utilized the torque generated by the unbalanced asymmetric gimbal frame, as shown in Fig. 3(b).

The physical behavior of a mirror can be described using a set of equations of motion. The sets of second-order differential equations describing the X-axis and y-rotation of the mirror and asymmetric gimbal frame can be obtained using the angular deflection, moment, damping coefficient, and angular spring constant. Figures 4 and 5 show the models of the rotational spring-mass-damper system for the X- and

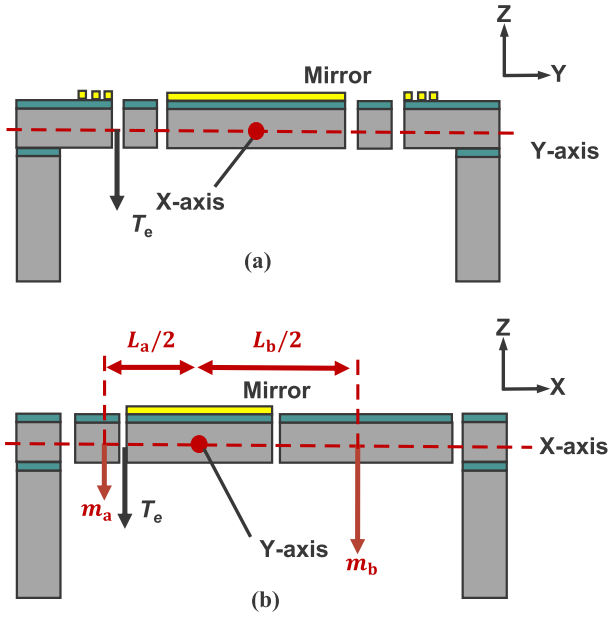

Fig. 3. (a) Schematic of X-axis rotation. The driving forces directly generate X-axis rotation. (b) Schematic of Y-axis rotation. The asymmetric gimbal frame converts these forces into Y-axis rotation.

Y-axes scanning modes. As shown in Figs. 4 and 5, the mirror was located at the end of the system and connected to the asymmetric gimbal frame in series. The mirror and asymmetric gimbal frame were described as inertial components and these components were supported by torsional beams.

The X-axis rotation can be described as

$$J_x\ddot{\theta_x} + c_x\dot{\theta_x} + k_x(\theta_x - \theta_1) = 0 \tag{1}$$

$$J_1\ddot{\theta_1} + c_1\dot{\theta_1} + (k_x + k_1)\theta_1 = T_e + k_x\theta_x \tag{2}$$

where J_x and J_1 are the inertial moments of the mirror and asymmetric gimbal frame, respectively, θ_x and θ_1 are the X-axis rotation angles of the mirror and asymmetric gimbal frame, respectively, c_x and c_1 are the viscosities of the mirror and asymmetric gimbal frames, respectively, k_x and k_1 are the spring constants of the two torsional beams, and Te is the torque generated by the electromagnetic actuator forces F_x and F_y. Under the X-axis rotation mode, the frame was symmetrical along the X-axis. Therefore, these moments were ignored.

However, the moments of the asymmetric gimbal frame must be considered in Y-axis rotation. The Y-axis rotation can be described as

$$J_y\ddot{\theta_y} + c_y\dot{\theta_y} + k_y(\theta_y - \theta_2) = 0 \tag{3}$$

$$J_2\ddot{\theta_2} + c_2\dot{\theta_2} + (k_y + k_2)\theta_2 = T_e + k_y\theta_y + m_a g L_a/2\cos\theta_2 - m_b g L_b/2\cos\theta_2 \tag{4}$$

where J_y and J_2 are the inertial moments of the mirror and asymmetric gimbal frame, respectively θ_y and θ_2 are the Y-axis rotation angles of the mirror and asymmetric gimbal frame, respectively, c_y and c_2 are the viscosities of the mirror and asymmetric gimbal frame, respectively, k_y and k_2 are the spring constants of the two torsional beams, and T_e is the torque generated by the forces of the electromagnetic actuators: F_x and F_y. Further, m_a and m_b are the masses of the short and long parts of the asymmetric gimbal frame, respectively. As shown in Eq. 4, the Y-axis rotation was

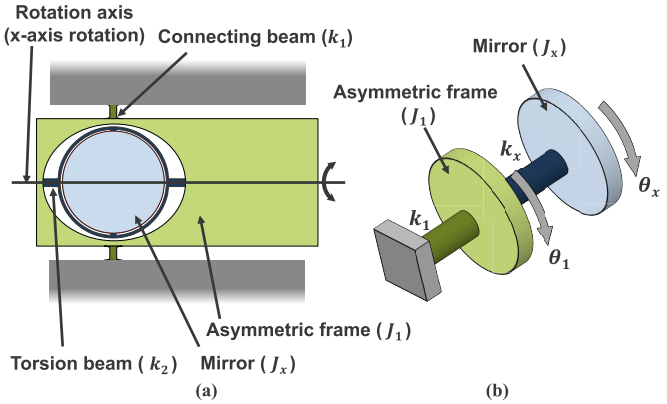

Fig. 4. (a) Schematic of the X-axis rotation and (b) rotational spring-mass–damper system model.

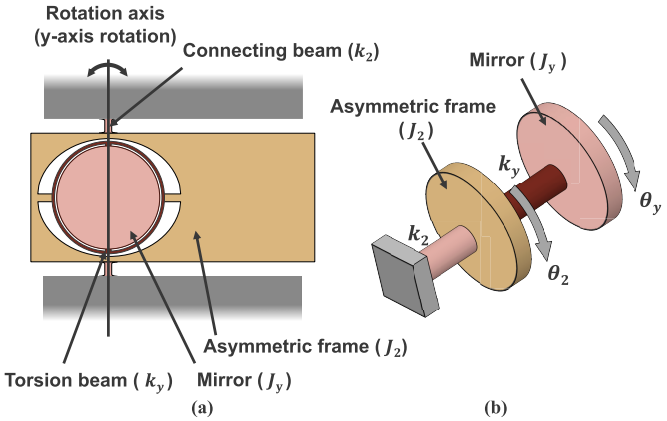

Fig. 5. (a) Schematic of the Y-axis rotation and (b) rotational spring-mass–damper system model.

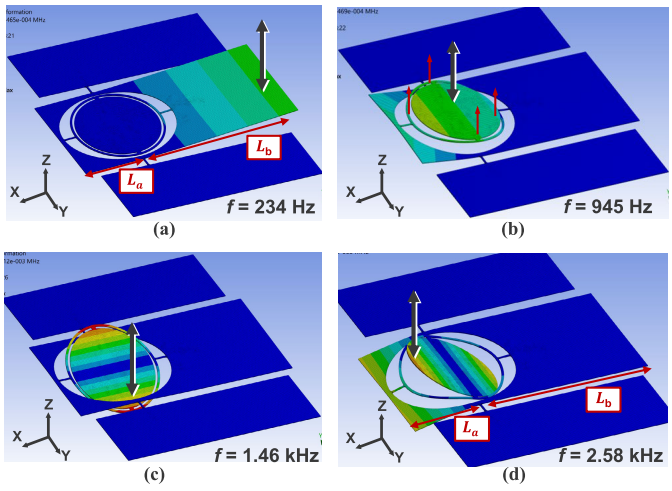

Fig. 6. FEM simulation results of various resonant modes of the proposed device. (a) Y-axis slow-resonant mode, where, primarily, the longer part of the frame part (L_b) undergoes rotation. (b) In the Z-axis piston resonant mode, the mirror part vibrates vertically. (c) X-axis resonant mode, where the mirror part primarily rotates. (d) Y-axis fast resonant mode, where, primarily, the mirror part rotates with a counter-rotation of the shorter part of the frame (L_a).

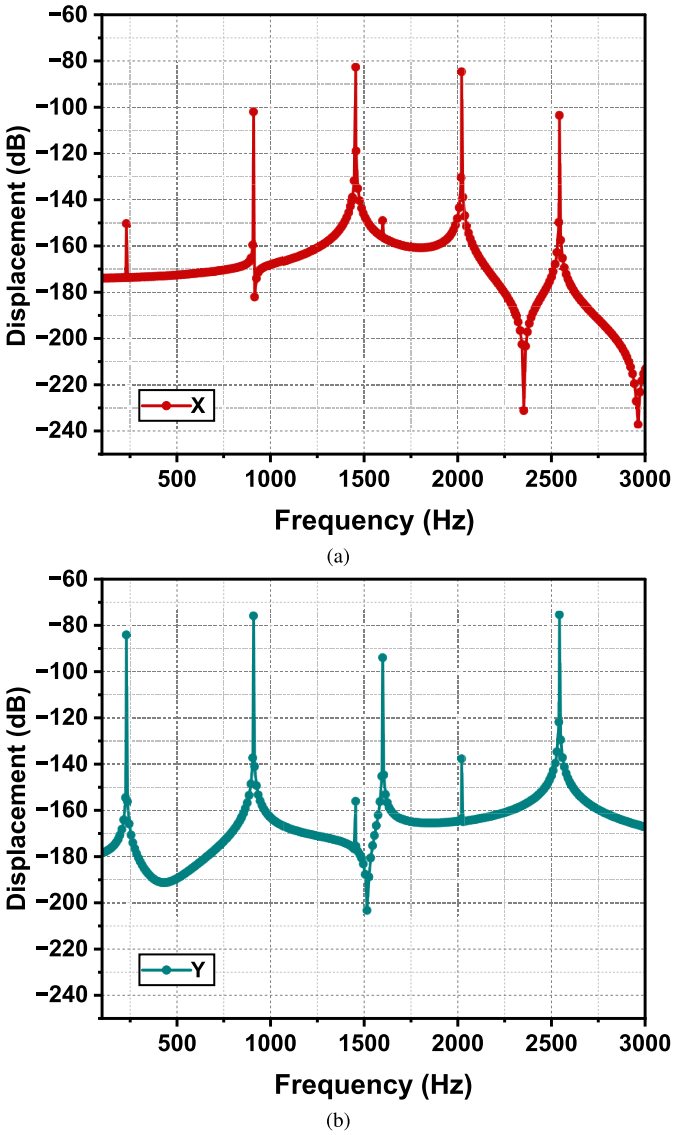

Fig. 7. FEM Simulation results of (a) X-axis and (b) Y-axis frequency responses of the mirror.

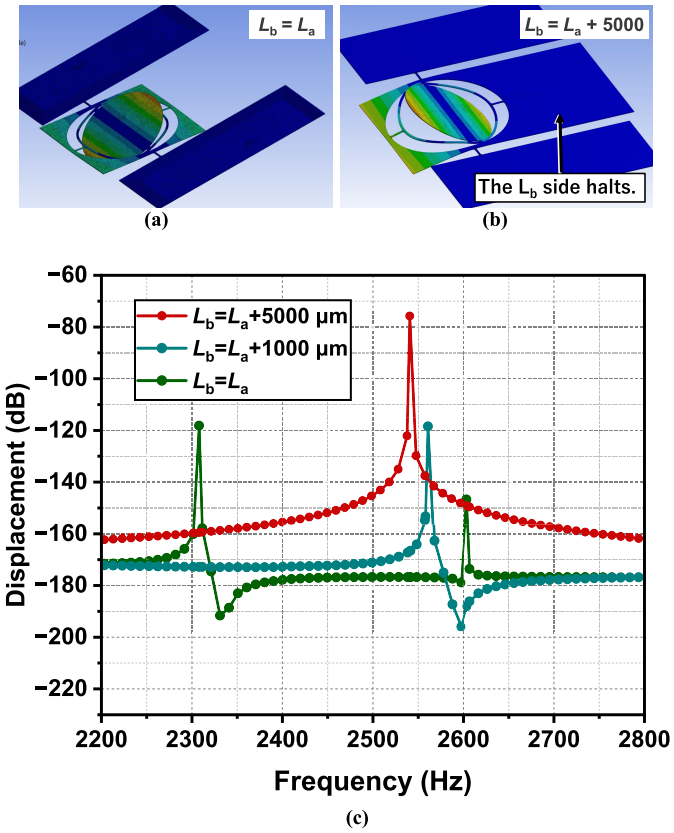

Fig. 8. Simulation model when (a) $L_b = L_a$ and (b) $L_b = L_a + 5000$. (c) FEM Simulation results of Y-axis rotation at the fast resonant mode when the asymmetric ratio was changed.

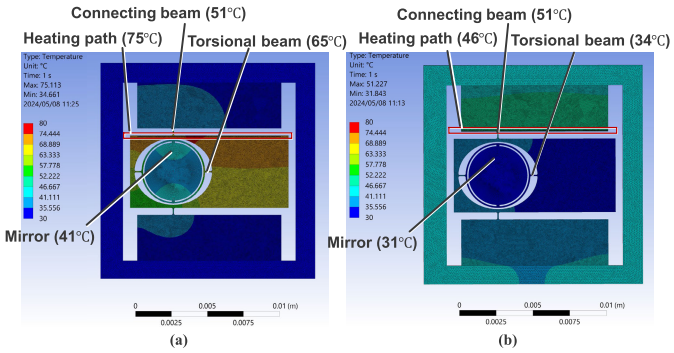

Fig. 9. FEM simulation results when we applied 100 mW heat flow under ambient temperature of 30 °C to the heating path (a) on the asymmetric gimbal frame and (b) outside the asymmetric gimbal frame.

dependent on the generated torque T_e and the moment owing to the asymmetric gimbal frame.

III. FEM Simulation

Figure 6 shows the various mode shapes of the proposed device derived from a finite element method (FEM) simulation using ANSYS Mechanical. The X-axis rotation mode was observed at 1.461 kHz, as shown in Fig. 6(c). In addition, at 945 Hz, the mirror vibrated vertically, which is called the piston resonant mode (Fig. 6(b)).

As shown in Figs. 6(a) and 6(d), two resonant modes (slow and fast) exist at 234 Hz and 2.582 kHz in the Y-axis rotation modes owing to the asymmetric gimbal frame. While the longer part of the asymmetric gimbal frame (L_b) primarily rotated in the slow-scan mode, the mirror component primarily rotated in the fast-scan mode. Note that the fast scan mode included a counter-rotation of the short part of the frame (L_a), depending on the mirror. As shown in 6(d), the longer part of the asymmetric gimbal frame (called the L_B part) was halted. This indicates that $m_b g L_b/2 \cos\theta_2$ on the right side of Eq. 4 decreased. In addition, J_2 and c_2 decreased owing to the decrease in the rotational mass and size. Consequently, rotation increased when an asymmetric gimbal frame was used. Figures 7(a) and 7(b) show the simulated results for the X- and Y-axis rotational frequency responses. We applied a frequency signal of 50 kPa amplitude in the Z direction to the current paths on one side of the cantilever, shown in Figs. 1 and 2. As shown in Fig. 7(b), the displacement of the mirror was largest in the Y-axis fast resonant mode, despite the highest-frequency resonant mode.

As shown in Fig. 6(b), the X- and Y-axes deflections were large at 945 Hz because of the piston-mode actuation.

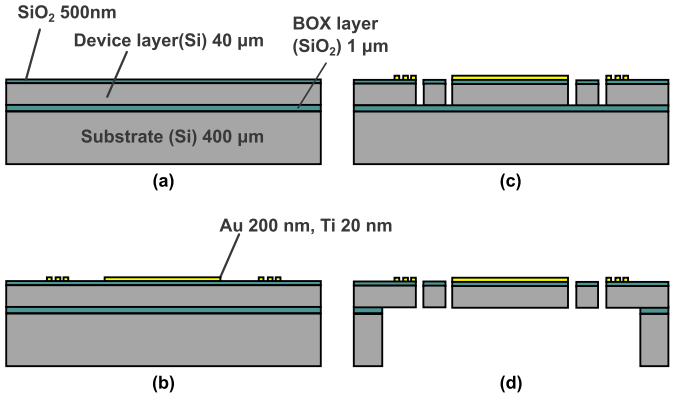

Fig. 10. Process flow of the proposed device. (a) Thermal oxidization and sputtering the titanium and gold. (b) Patterning the titanium and gold for current paths. (c) Patterning SiO_2 layer and DRIE of the device layer. (d) DRIE of the substrate followed by release of the device by etching the BOX layer using CHF_3 plasma.

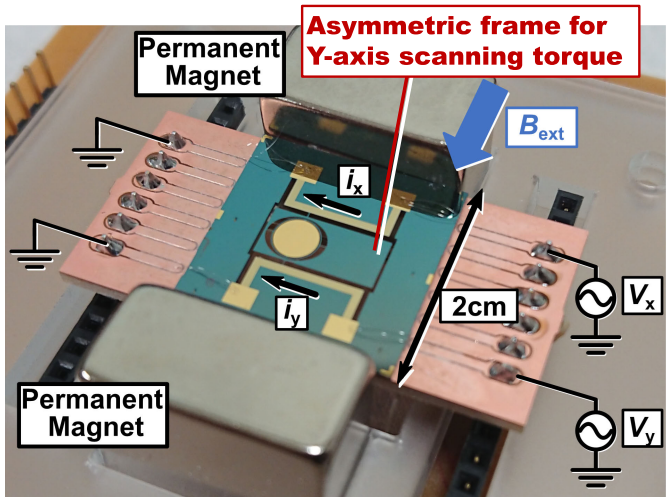

Fig. 11. Image of the fabricated device with external permanent magnets.

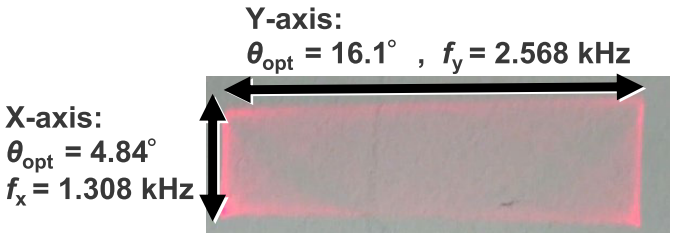

Fig. 12. Scanned Lissajou's pattern using the X- and Y-axes fast resonant mode. Each current was applied independently, and both currents were 300 mA.

At 1.46 kHz, the X-axis deflection was the largest, as shown in Fig. 6(c). As shown in Figs 7(a) and 7(b), the X-axis displacement increased at the Y-axis resonant frequency. This was because of the nature of the cantilever actuator, which rotated along the Y-axis. However, these crosstalk displacements at the Y-axis resonant frequencies were more than 20 dB smaller than the X-axis resonant displacement. The Y-axis slow-resonant mode at 245 Hz and the Y-axis fast-resonant mode at 2.58 kHz, corresponding to Figs. 6(a) and 6(d) were observed, as shown in Fig. 7(b). The Y-axis displacement was the largest at a fast resonant-mode frequency of 2.58 kHz, owing to the proposed asymmetric gimbal frame.

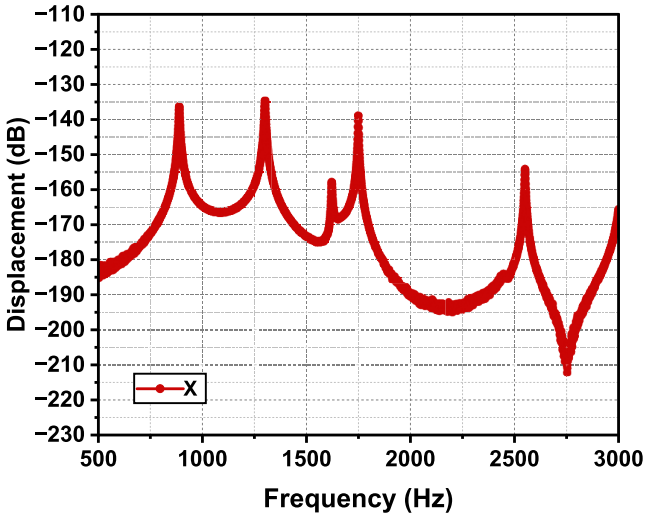

(a)

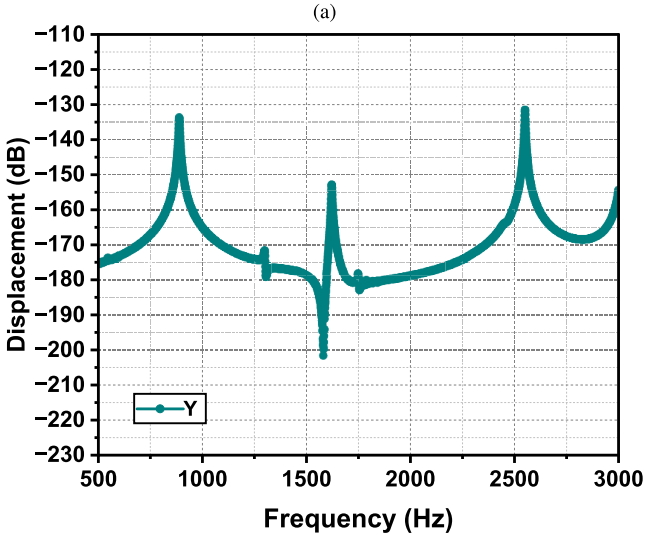

(b)

Fig. 13. Measured frequency response of (a) X-axis and (b) Y-axis scans using a laser-Doppler instrument when the 100 mA current was applied.

To investigate the role of the asymmetric gimbal frame, we swept the ratio of L_a to L_b. Figures 8(a) and 8(b) show the fast resonant mode displacement along the Y-axis fast resonant mode of the simulated models with $L_b = L_a$ and $L_b = L_a+5000$, respectively. Figure 8(b) shows the simulated results for Y-axis rotation using different L_b-L_a ratio models. Three different models were simulated: $L_b = L_a$, $L_b = L_a+1000$ μ m and $L_b = L_a + 5000$ μ m. As shown in Fig. 8(b), the deflection increased with increasing asymmetry ratio under the fast resonant mode of the Y axis.

Furthermore, we compared two different models with different placements of the heating path to observe the heat dissipation of the device when we applied 100 mW heat flow to the heating path (that is, simulated current path) at an ambient temperature of 30 °C, as shown in Fig. 9.

Figure 9(a) shows the thermal simulation model, where the heating path was placed on the asymmetric gimbal frame, which is similar to the placement of the previous two-axis electromagnetic scanner [13], [14]. The mesh element sizes of the device area and the outer bulk handle frame were 30 μ m and 50 μ m, respectively. The nodes of the element

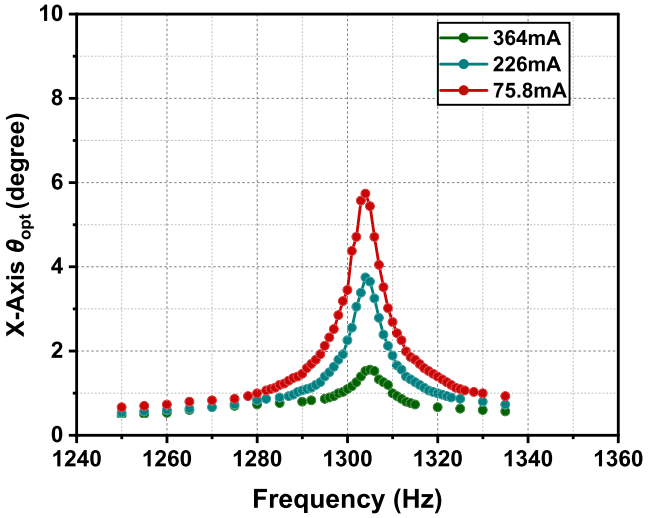

(a)

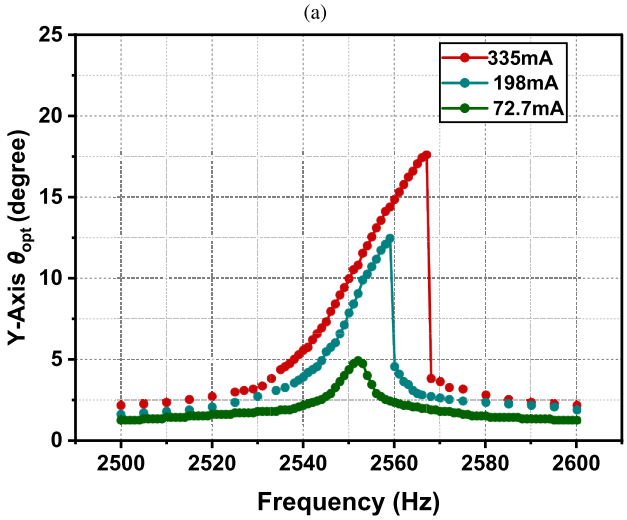

(b)

Fig. 14. Measured frequency response of (a) X-axis and (b) Y-axis scanning angles when the applied currents were changed.

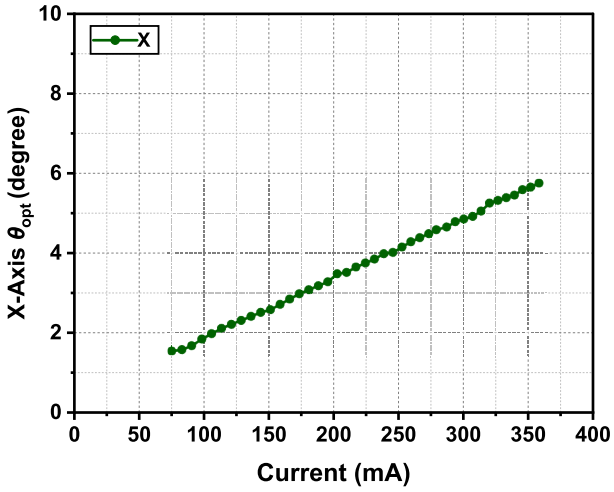

(a)

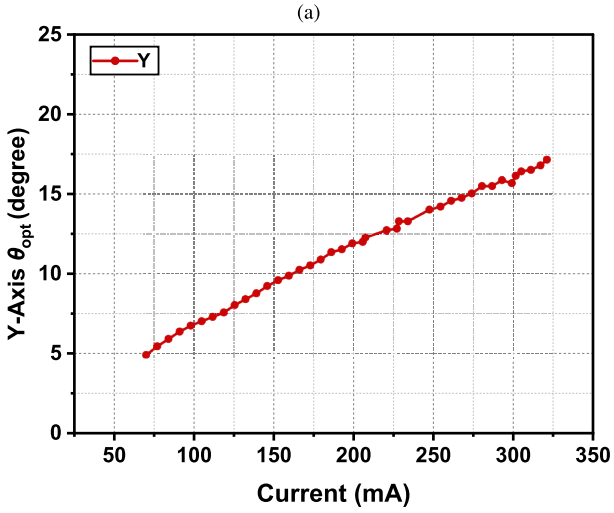

(b)

Fig. 15. Measured resonant scanning angles of X-axis and Y-axis scans when the applied currents were changed.

between the device area and the outer bulk handle frame were continuous. The mesh size was the smallest that could be simulated in the used environment. We confirmed that the mesh quality was enough to obtain accurate results because the results remained the same when using the larger mesh element sizes. As shown in Fig. 9(a), the maximum temperature around the heating path was 75 °C, the connecting beam was 51 °C, and the torsional beam was 65 °C. On the other hand, in the model, as shown in Fig. 9(b), the heating path was placed outside the asymmetric gimbal frame, which simulates the proposed design. In this model, the maximum temperature around the heating path was 51 °C, the connecting beam was 46 °C, and the torsional beam was 34 °C. We consider this to be another advantage of the proposed position of coils in the proposed design.

IV. Fabrication

Figure 10 illustrates the process flow of the proposed device. We used a 6-inch 40 μ m-1 μ m-400 μ m SOI wafer as substrate. First, the wafer was oxidized to form an insulating layer with a thickness of 500 nm, as shown in Fig. 10(a). Subsequently, 20-nm thick Ti and 200-nm thick Au were sputtered for current paths. The Au and Ti were etched using an Au etchant (KANTO CHEMICAL AURUM-302) and 5% ammonia peroxide mixture (APM), as shown in Fig. 10(b). Subsequently, the SiO_2 layer was etched using a CHF_3 plasma, and the 40 μ m device Si layer was etched using deep reactive ion etching (DRIE), as shown in Fig. 10(c). Subsequently, the back of the substrate was etched by DRIE. Finally, the moving structures were released by etching the BOX layer using CHF_3 plasma, as shown in Fig. 10(d). The chips were separated by DRIE and release-etching of the BOX layer using CHF_3 plasma. Figure 11 illustrates the fabricated device.

V. Measurement

As shown in Fig 11, we placed two external Neodymium magnets (2 cm high, 2 cm wide, 1 cm thick) on each side of the device to generate B_{ext}. The magnets were mechanically fixed to the PCB using a 5 mm thick acrylic sheet jig, as shown in Fig. 11. Figure 12 shows the scanned Lissajous pattern. The currents were applied independently at 300 mA. The optical scanning angles were 4.84° for the 1.308 kHz X-axis and 16.1° for 2.568 kHz Y-axis scans, respectively.

Figures 13(a) and 13(b) show the frequency responses of the X- and Y-axes scans measured using a laser Doppler instrument (Polytec Inc., MSA-500), respectively. In this measurement, the current was limited to 100 mA due to the measurement limitations of the laser Doppler instrument. As shown in Figs. 13(a) and 13(b), the X- and Y-axes resonant mode frequencies were 1.308 and 2.568 kHz, respectively.

Figures 14(a) and 14(b) show the frequency dependence of the X- and Y-axes scanning angles, respectively, around the operating resonant frequency when the applied current was changed. We swept the driving-signal frequency from low to high. As shown in Fig. 14(a), the resonance behavior and applied current were linear. However, as shown in Fig. 14 (b), non-linear behavior was observed owing to a spring stiffening increase in resonance frequency at larger deflections caused by a progressive spring characteristic. Figures 15(a) and 15(b) show the relationship between the maximum scanning angle and the applied current.

VI. Conclusion

This study proposed a two-axis resonant electromagnetic scanner with an asymmetric gimbal frame that generates two-axis torques from a one-axis lateral external magnetic field and can save the packaging size. Two driving forces were generated by two independent electromagnetic actuators placed on both sides of the asymmetric gimbal frame, which converted the unidirectional forces into two-axis torques. We successfully demonstrated biaxial scanning using the proposed device with a 4 mm mirror and a one-axis lateral magnetic field. The optical scanning angles were 4.84° and 16.1° for the 1.308 kHz X-axis and 2.568 kHz Y-axis scan, respectively, when a current of 300 mA was applied independently to the X- and Y-axis driving actuators. The results indicated that the proposed method reduced the packaging size of the electromagnetic scanner without performance degradation.

However, the scanning angles were not wide, compared to the previous electromagnetic scanners. We consider that the thin layer of current paths limits the maximum current, which causes the small scanning angles. Future work is to realize the proposed scanner with the thicker current paths deposited by electroplating.

Acknowledgment

The patterning of the device was carried out using open facilities maintained by the Nanotechnology Platform Program of MEXT and the University of Tokyo, and the photomask was fabricated using the System Design Laboratory. (d. lab) 8-inch EB writer F5112+VD01 donated by Advantest Corporation.

References

[1] S. T. S. Holmström, U. Baran, and H. Urey, "MEMS laser scanners: A review," *J. Microelectromech. Syst.*, vol. 23, no. 2, pp. 259–275, Apr. 2014.

[2] L. Liu, E. Wang, X. Zhang, W. Liang, X. Li, and H. Xie, "MEMS-based 3D confocal scanning microendoscope using MEMS scanners for both lateral and axial scan," *Sens. Actuators A, Phys.*, vol. 215, pp. 89–95, Aug. 2014.

[3] W. O. Davis, R. Sprague, and J. Miller, "MEMS-based pico projector display," in *Proc. IEEE/LEOS Int. Conf. Opt. MEMs Nanophotonics*, Aug. 2008, pp. 31–32.

[4] Q. Hu, C. Pedersen, and P. J. Rodrigo, "Eye-safe diode laser Doppler LiDAR with a MEMS beam-scanner," *Opt. Exp.*, vol. 24, no. 3, pp. 1934–1942, Feb. 2016.

[5] F. Senger et al., "Centimeter-scale MEMS scanning mirrors for high power laser application," *Proc. SPIE*, vol. 9375, Feb. 2015, Art. no. 937509.

[6] S. Inagaki, Y. Okamoto, A. Higo, and Y. Mita, "High-resolution piezoelectric MEMS scanner fully integrated with focus-tuning and driving actuators," in *Proc. 20th Int. Conf. Solid-State Sensors, Actuat. Microsystems Eurosensors XXXIII (TRANSDUCERS EUROSENSORS XXXIII)*, Jun. 2019, pp. 474–477.

[7] Y. Okamoto et al., "High-uniformity centimeter-wide Si etching method for MEMS devices with large opening elements," *Jpn. J. Appl. Phys.*, vol. 57, no. 4S, Mar. 2018, Art. no. 04FC03.

[8] H. M. Chu and K. Hane, "Design, fabrication and vacuum operation characteristics of two-dimensional comb-drive micro-scanner," *Sens. Actuators A, Phys.*, vol. 165, no. 2, pp. 422–430, Feb. 2011.

[9] C.-D. Chen, Y.-J. Wang, and P. Chang, "A novel two-axis MEMS scanning mirror with a PZT actuator for laser scanning projection," *Opt. Exp.*, vol. 20, no. 24, pp. 27003–27017, Nov. 2012.

[10] T. Naono, T. Fujii, M. Esashi, and S. Tanaka, "Non-resonant 2-D piezoelectric MEMS optical scanner actuated by Nb doped PZT thin film," *Sens. Actuators A, Phys.*, vol. 233, pp. 147–157, Sep. 2015.

[11] Y. Okamoto, S. Gorwadkar, Y. Takei, and H. Okada, "3.8×3.8 mm^2 tiny piezoelectric resonant MEMS scanner using fork-shaped and ring-shaped actuators," in *Proc. IEEE 37th Int. Conf. Micro Electro Mech. Syst. (MEMS)*, Jan. 2024, pp. 162–165.

[12] N. Asada, H. Matsuki, K. Minami, and M. Esashi, "Silicon micromachined two-dimensional galvano optical scanner," *IEEE Trans. Magn.*, vol. 30, no. 6, pp. 4647–4649, Nov. 1994.

[13] A. D. Yalcinkaya, H. Urey, D. Brown, T. Montague, and R. Sprague, "Two-axis electromagnetic microscanner for high resolution displays," *J. Microelectromech. Syst.*, vol. 15, no. 4, pp. 786–794, Aug. 2006.

[14] A. R. Cho et al., "Electromagnetic biaxial microscanner with mechanical amplification at resonance," *Opt. Exp.*, vol. 23, no. 13, pp. 16792–16802, Jun. 2015.

[15] D. D. H. Tran et al., "2-DOF MEMS mirror with large mechanical angles using one magnetic field for close range scanning applications," in *Proc. 22nd Int. Conf. Solid-State Sensors, Actuat. Microsystems (Transducers)*, Jun. 2023, pp. 839–841.

[16] Y. Hua, S. Wang, B. Li, G. Bai, and P. Zhang, "Dynamic modeling and anti-disturbing control of an electromagnetic MEMS torsional micromirror considering external vibrations in vehicular LiDAR," *Micromachines*, vol. 12, no. 1, p. 69, Jan. 2021.

[17] Y. Park, S. Moon, J. Lee, K. Kim, S.-J. Lee, and J. Hyun Lee, "Via-less two-axis electromagnetic micro scanner based on dual radial magnetic fields," *IEEE Photon. Technol. Lett.*, vol. 30, no. 5, pp. 443–446, Mar. 1, 2018.

[18] K. H. Koh and C. Lee, "A two-dimensional MEMS scanning mirror using hybrid actuation mechanisms with low operation voltage," *J. Microelectromech. Syst.*, vol. 21, no. 5, pp. 1124–1135, Oct. 2012.

[19] Y. Okamoto, T.-V. Nguyen, H. Okada, and M. Ichiki, "Via-less two-axis electromagnetic scanner using an asymmetric frame on a one-axis lateral magnetic field," in *Proc. IEEE 35th Int. Conf. Micro Electro Mech. Syst. Conf. (MEMS)*, Jan. 2022, pp. 967–970.

[20] Y. Okamoto, H. Okada, and M. Ichiki, "Two-axis electromagnetic scanner integrated with an electrostatic XY-stage positioner," in *Proc. IEEE 36th Int. Conf. Micro Electro Mech. Syst. (MEMS)*, Jan. 2023, pp. 41–44.

Yuki Okamoto (Member, IEEE) received the B.E., M.E., and Ph.D. degrees in electrical engineering from The University of Tokyo, Japan, in 2015, 2017, and 2020, respectively. He is currently a Researcher with the Sensing System Research Center (SSRC), National Institute of Advanced Industrial Science and Technology (AIST), Tsukuba, Japan. He has engaged in research projects to develop a high-performance MEMS scanner and a piezoelectric MEMS micropump. His research interests include CMOS-MEMS sensors and actuators, particularly in free-space optical devices, such as MEMS scanners for light detection and ranging (LiDAR) and integrated microfluidics for lab-on-a-chip and μ TAS applications.

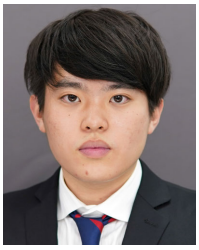

Rihachiro Nakashima (Graduate Student Member, IEEE) received the B.E. and M.E. degrees in mechanical engineering from Keio University, Japan, in 2021 and 2023, respectively, where he is currently pursuing the Ph.D. degree with the Graduate School of Integrated Design Engineering. He is also a Research Assistant with the Sensing System Research Center (SSRC), National Institute of Advanced Industrial Science and Technology (AIST), Tsukuba, Japan. His research interests include the MEMS physical sensor fabrication using laser processing and their applications.

Ryo Oda received the B.E. degree in mechanical engineering from Keio University, Japan, in 2023, where he is currently pursuing the M.E. degree with the Graduate School of Integrated Design Engineering. He is also a Research Assistant with the Sensing System Research Center (SSRC), National Institute of Advanced Industrial Science and Technology (AIST), Tsukuba, Japan. His research interests include MEMS sensors and laser-induced graphene (LIG), especially MEMS pressure sensors and force plates for droplet measurement.

Thanh-Vinh Nguyen received the B.E., M.E., and Ph.D. degrees in mechano-informatics from The University of Tokyo, Japan, in 2010, 2012, and 2015, respectively. He was a Researcher with the Sensing System Research Center (SSRC), National Institute of Advanced Industrial Science and Technology (AIST), Tsukuba, Japan. Currently, he is with Form Factors Inc., USA. His research interests include MEMS-based force sensor, acoustic sensor, droplet dynamics, and wearable health monitoring.

Yusuke Takei (Member, IEEE) received the Ph.D. degree in mechano-informatics from the Graduate School of Information Science and Technology, The University of Tokyo, in 2008. From 2008 to 2017, he was with the Department of Mechano-Informatics, Graduate School of Information Science and Technology, The University of Tokyo, as a Project Assistant Professor. He is currently a Team Leader of the Hybrid Sensing Device Team, Sensing System Research Center (SSRC), National Institute of Advanced Industrial Science and Technology (AIST). His research interests include MEMS sensors and their application, especially in the biometric field.

Masaaki Ichiki received the B.E., M.E., and Ph.D. degrees in applied physics from Waseda University, Japan, in 1990, 1992, and 1996, respectively. He is currently the Deputy Director and a Team Leader with the Sensing System Research Center (SSRC), National Institute of Advanced Industrial Science and Technology (AIST), Tsukuba, Japan. He has engaged in research projects to develop a useful sensor fusion systems, including smart materials, for applications in a smart society. His research interests include solid-state material physics and its applications, particularly smart materials, including the preparation of ferroelectric and piezoelectric materials and their applications in the field of IoT sensing.

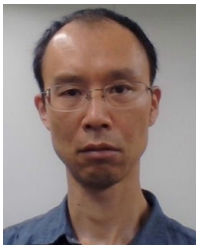

Hironao Okada received the B.E. degree in materials science and engineering from Kyoto University in 2001 and the M.E. and Ph.D. degrees in precision engineering from The University of Tokyo in 2003 and 2007, respectively. After working as a Researcher with The University of Tokyo for one year, he became a Researcher with the National Institute of Advanced Industrial Science and Technology (AIST) in 2008, where he is currently a Senior Researcher with the Sensing System Research Center. His research interests include wireless sensor network systems, low-power wireless communication technologies, and electrochemical sensors for monitoring biological information.